

Generalized parameter-space metrics for continuous gravitational-wave searches

P. B. Covas^{1,2,*} and R. Prix²

¹*Departament de Física, Universitat de les Illes Balears,
IAC3 – IEEC, Carretera Valldemossa km 7.5, E-07122 Palma, Spain*

²*Max Planck Institute for Gravitational Physics (Albert Einstein
Institute) and Leibniz Universität Hannover, D-30167 Hannover, Germany*

Many searches for continuous gravitational waves face significant computational challenges due to the need to explore large parameter spaces characterized by unknown parameters. Parameter-space metrics are used to predict the relative loss of signal power when the searched parameters differ from the true signal parameters. In this paper we present generalized parameter-space metrics for the \mathcal{F} -statistic (a detection statistic used in many searches) that improve upon previous idealized metrics by incorporating realistic effects such as data gaps and varying noise floors. We derive a new marginalized \mathcal{F} -statistic metric that is more accurate than the previous averaged \mathcal{F} -statistic metric, especially for short coherent segments. We also derive a more accurate semi-coherent metric that properly accounts for the signal-power variability over segments. We provide numerical tests illustrating that the new generalized metrics provide more accurate mismatch predictions than previous expressions. More accurate metrics can result in a reduced number of templates needed for a given search, a feature that could improve the sensitivity of future searches.

I. INTRODUCTION

Continuous gravitational waves (CWs) are long-lasting and almost monochromatic gravitational waves (yet to be detected) that can be emitted by different sources, such as asymmetric (around their rotation axis) rotating neutron stars [1]. Searches for CWs can have different targets, such as known pulsars or unknown neutron stars in our galaxy (commonly called all-sky searches).

In order to discern whether a dataset contains an astrophysical signal or just noise, a detection statistic that is compared to a threshold is commonly computed. One of these detection statistics is the \mathcal{F} -statistic [2, 3], which is obtained after analytical maximization (over the four amplitude parameters that describe a typical CW signal) of the log-likelihood ratio. This detection statistic has been used in many CW searches (see [4] for a recent review). Due to the prohibitive computational cost of some searches, the data can be divided in many shorter segments and a semi-coherent version of the \mathcal{F} -statistic might be used [5].

The typical CW signal model includes parameters that for some searches are unknown, such as the rotational frequency or the sky position. These unknown parameters have to be explicitly explored with a template bank or with a stochastic sampling algorithm. The parameter-space metric is a second-order approximation that aims to predict the relative loss of signal power (also called mismatch) incurred when these searched parameters are not equal to the true parameters of a putative astrophysical signal [6].

The full coherent parameter-space metric for the (multi-detector) \mathcal{F} -statistic was first derived in [6]. The different metrics derived there are subject to some idealizations, such as (i) the data is assumed to have no

gaps, i.e., a duty cycle of 100%; (ii) the noise floor of each detector, quantified in terms of the amplitude spectral density (ASD), is assumed to be constant over time. Furthermore, the semi-coherent metric (cf. [5, 7, 8]) for the \mathcal{F} -statistic has so far been derived under the assumption of (iii) equal signal power over segments. However, realistic datasets typically have an overall duty cycle less than 100% (usually around $\sim 70\%$), and varying duty cycles and noise floors over time, as shown in Fig. 1 for the O3 observing run [9, 10] of the Advanced LIGO gravitational-wave detectors located in Hanford (H1) and Livingston (L1) [11]. In this paper we attempt to study the behavior of the \mathcal{F} -statistic parameter-space metrics when these assumptions do not hold, and derive generalized expressions and implementations that take these effects into account.

The parameter-space metric can be used to optimally construct a template grid [12, 13], and since the sensitivity of some CW searches is bounded by a limited computational budget, placing templates in a more accurate way (due to more accurate mismatch predictions) is an important topic of research [14]. There are more reasons why obtaining more accurate parameter-space metrics is relevant for CW searches, such as (i) better analytical estimations of the uncertainty on the unknown parameters (see for example [15]) without having to carry out expensive Bayesian parameter estimation analyses; (ii) optimal setup algorithms (such as [14]) could indicate that discarding some fraction of the less sensitive data can be beneficial, and the resulting dataset would have a lower duty cycle, thus making the usage of more realistic metrics more relevant; (iii) use jump proposals (within Bayesian stochastic sampling algorithms such as [16]) based on the Fisher information matrix, which is proportional to the parameter-space metric; (iv) compare the resulting posteriors from a Bayesian stochastic sampling analysis with Fisher matrix predictions for validation tests.

* jb.covas@uib.es

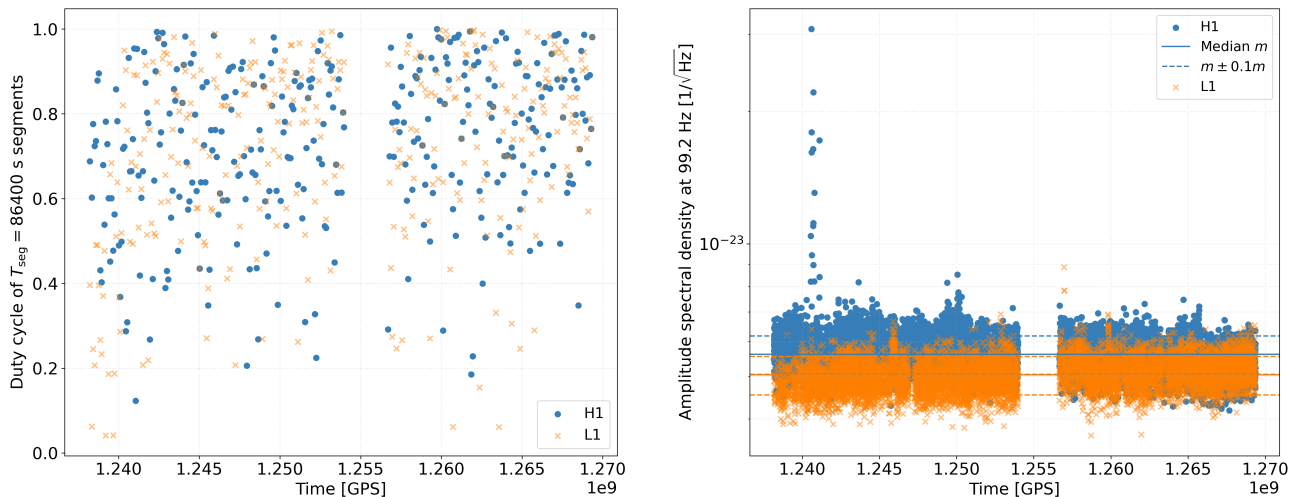


FIG. 1: The left plot shows the duty cycle of the O3 observing run for each segment of $T_{\text{seg}} = 86400$ s as a function of the segment mid-time for each detector. The right plot shows the amplitude spectral density (at 99.2 Hz) of the O3 observing run for each SFT as a function of the SFT mid-time, while the horizontal (dashed) lines show the median m ($m \pm 0.1$) for each detector. SFTs of 1800 s have been used, which have been modified with a time-domain cleaning algorithm [17]. The different markers show the detectors H1 (blue circles) and L1 (orange crosses).

The main results of this paper are: (i) we derive an expression for the metric where data gaps and a varying noise floor are taken into account, and we implement this expression numerically; (ii) we present a new expression for a marginalized (over the unknown amplitude parameters) \mathcal{F} -statistic metric; (iii) we derive an expression for the semi-coherent metric that properly takes into account the variability of the signal power across different segments by applying weights, and we derive the correct expression for detection statistics that are weighted, such as the one proposed in [18]. We test all of these new expressions and show that they are able to predict the mismatch more accurately than the previous expressions for realistic datasets.

This paper is organized in the following way: in Sec. II we give an introduction to the \mathcal{F} -statistic and to parameter-space metrics; in Sec. III we derive the expressions for the new generalized parameter-space metrics; in Sec. IV we show the improved accuracy of the new metrics through diverse numerical tests; in Sec. V we summarize the paper, present our conclusions, and advance some ideas for future research.

II. BACKGROUND

In this section we introduce the basic framework and notation for the \mathcal{F} -statistic and its associated parameter-space metrics.

A. The \mathcal{F} -statistic

In order to detect CWs, we compare two main hypotheses about the data $x(t)$, where t is the time in the detector frame:

- noise hypothesis: the data only consists of Gaussian noise, $x(t) = n(t)$.
- signal hypothesis: in addition to Gaussian noise, the data consists of a CW signal $s(t; \mathcal{A}_s, \lambda_s)$ parametrized by four amplitude parameters \mathcal{A}_s and a number of phase-evolution parameters λ_s , i.e., $x(t) = n(t) + s(t; \mathcal{A}_s, \lambda_s)$.

The CW signal can be expressed in terms of four basis functions h_μ in the form:

$$s(t; \mathcal{A}_s, \lambda_s) = \sum_{\mu=1}^4 \mathcal{A}_s^\mu h_\mu(\lambda_s), \quad (1)$$

where $\mathcal{A}^\mu(h_0, \cos \iota, \psi, \phi_0)$ are the JKS amplitude parameters [2, 19] depending on the overall signal amplitude h_0 , polarization angles $\cos \iota$ and ψ , and the initial phase ϕ_0 . The four basis functions h_μ are

$$h_1 = a(t) \cos \phi(t), \quad h_2 = b(t) \cos \phi(t), \quad (2)$$

$$h_3 = a(t) \sin \phi(t), \quad h_4 = b(t) \sin \phi(t), \quad (3)$$

where $a(t)$ and $b(t)$ are the antenna pattern functions (see [2, 19]), and $\phi(t)$ is the phase of the signal in the detector frame, parameterized by the phase-evolution parameters λ such as the rotational frequency f_0 , spin-downs

f_1, f_2, \dots , the sky position, and (if applicable) binary orbital parameters.

The log-likelihood ratio between signal and noise hypotheses in this form is found to depend quadratically on the JKS amplitude parameters \mathcal{A}^μ of the template and can thus be analytically maximized (reducing the computational cost), which yields the well-known \mathcal{F} -statistic [2, 3, 20]:

$$2\mathcal{F}(x; \lambda) = x_\mu \mathcal{M}^{\mu\nu} x_\nu, \quad (4)$$

with implicit summation over repeated $\mu, \nu = 1, \dots, 4$. Here we used the definitions

$$x_\mu \equiv (x|h_\mu), \quad \mathcal{M}_{\mu\nu} \equiv (h_\mu|h_\nu), \quad (5)$$

in terms of the multi-detector scalar product [3, 19], which for uncorrelated noise between detectors and a narrow-band signal with flat noise floor in the signal band f can be written as

$$(x|y) \equiv 2\gamma \langle xy \rangle, \quad (6)$$

where we have defined the *data factor* γ as

$$\gamma \equiv \mathcal{S}^{-1} T_{\text{data}}, \quad (7)$$

with the total amount of data $T_{\text{data}} \equiv N_{\text{SFTs}} T_{\text{SFT}}$ in terms of the number N_{SFTs} and duration T_{SFT} of short Fourier transforms¹ (SFTs). The overall noise floor \mathcal{S} at frequency f is defined as

$$\mathcal{S}^{-1} \equiv \frac{1}{N_{\text{SFTs}}} \sum_{X\alpha} \mathcal{S}_{X\alpha}^{-1}, \quad (8)$$

in terms of the per-SFT power-spectral densities $\mathcal{S}_{X\alpha}$, where α is an index over SFTs of detector X . We define the time-averaging operation as

$$\langle xy \rangle \equiv \frac{1}{N_{\text{SFTs}}} \sum_{X\alpha} \frac{w_{X\alpha}}{T_{\text{SFT}}} \int_{t_{X\alpha} - T_{\text{SFT}}/2}^{t_{X\alpha} + T_{\text{SFT}}/2} x_X(t) y_X(t) dt, \quad (9)$$

where the timestamps $t_{X\alpha}$ refer to the middle of an SFT. The per-SFT noise weights $w_{X\alpha}$ in this expression are defined as

$$w_{X\alpha} \equiv \frac{\mathcal{S}_{X\alpha}^{-1}}{\mathcal{S}^{-1}}, \quad (10)$$

with normalization

$$\sum_{X\alpha} w_{X\alpha} = N_{\text{SFTs}}, \quad (11)$$

as can be seen from Eq. (8).

The \mathcal{F} -statistic follows a non-central χ^2 -distribution with an expectation value of

$$E[2\mathcal{F}(x; \lambda)] = 4 + \rho^2(\mathcal{A}_s, \lambda_s; \lambda), \quad (12)$$

with the non-centrality parameter defining the *signal power* $\rho^2(\mathcal{A}_s, \lambda_s; \lambda)$. In the perfect-match case, where the phase-evolution parameters of the template λ match those of the signal λ_s , the signal power can be expressed [22] as:

$$\rho_0^2 \equiv \rho^2(\mathcal{A}_s, \lambda_s; \lambda_s) = (s|s) = h_0^2 \gamma g^2, \quad (13)$$

where we used the definition of the geometric response function g of [23], namely

$$g^2(\hat{n}, \cos \iota, \psi) \equiv \alpha_1 A + \alpha_2 B + 2\alpha_3 C, \quad (14)$$

where \hat{n} is the sky position, the amplitude angle factors $\alpha_k(\cos \iota, \psi)$ are defined as:

$$\begin{aligned} \alpha_1 &\equiv \frac{1}{4} (1 + \cos^2 \iota)^2 \cos^2 2\psi + \cos^2 \iota \sin^2 2\psi, \\ \alpha_2 &\equiv \frac{1}{4} (1 + \cos^2 \iota)^2 \sin^2 2\psi + \cos^2 \iota \cos^2 2\psi, \\ \alpha_3 &\equiv \frac{1}{4} (1 - \cos^2 \iota)^2 \sin 2\psi \cos 2\psi, \end{aligned} \quad (15)$$

and $\gamma A \equiv \mathcal{M}_{11} = \mathcal{M}_{33}$, $\gamma B \equiv \mathcal{M}_{22} = \mathcal{M}_{44}$, and $\gamma C \equiv \mathcal{M}_{12} = \mathcal{M}_{34}$ are the (non-negligible) components of the (symmetric) antenna-pattern matrix $\mathcal{M}_{\mu\nu}$ defined in Eq. (5), with

$$A = \langle a^2 \rangle, \quad B = \langle b^2 \rangle, \quad C = \langle ab \rangle, \quad (16)$$

and the sub-determinant $D \equiv AB - C^2$.

Due to the high computational cost of wide-parameter-space CW searches, these typically use semi-coherent methods, where the data will be divided into N_{seg} segments of duration T_{seg} each, and the four signal amplitude parameters \mathcal{A}^μ are required to be constant only within each segment, resulting in the semi-coherent $\widehat{\mathcal{F}}$ -statistic [5, 24] as a sum of coherent \mathcal{F} -statistics over segments. This was generalized in [18] to the *weighted* semi-coherent $\widehat{\mathcal{F}}_w$ -statistic, defined as

$$2\widehat{\mathcal{F}}_w(x; \lambda) \equiv \sum_{\ell=1}^{N_{\text{seg}}} w_\ell 2\mathcal{F}_\ell(x; \lambda), \quad (17)$$

where \mathcal{F}_ℓ is the coherent \mathcal{F} -statistic in segment ℓ and w_ℓ is the per-segment weight, with standard normalization (to have unit mean):

$$\sum_{\ell=1}^{N_{\text{seg}}} w_\ell = N_{\text{seg}}. \quad (18)$$

Dropping the per-segment weights recovers the classic semi-coherent \mathcal{F} -statistic $2\widehat{\mathcal{F}}(x; \lambda)$. As discussed in [18], a good choice of weights is empirically found as

$$w_\ell = k \gamma_\ell (A_\ell + B_\ell), \quad (19)$$

¹ SFTs [21] are a typical format for the input data of CW searches. We assume stationary noise and constant antenna-pattern coefficients over the duration of each SFT.

where the normalization k is fixed by Eq. (18). This (weighted) semi-coherent \mathcal{F} -statistic follows a (*generalized*) non-central χ^2 -distribution with an expectation value of (assuming that all segments have four degrees of freedom)

$$\begin{aligned} E \left[2\widehat{\mathcal{F}}_w(x; \lambda) \right] &= \sum_{\ell=1}^{N_{\text{seg}}} w_{\ell}(4 + \rho_{\ell}^2) \\ &= 4N_{\text{seg}} + \widehat{\rho}_w^2, \end{aligned} \quad (20)$$

where ρ_{ℓ}^2 is the signal power in segment ℓ and we have defined the (weighted) semi-coherent signal power $\widehat{\rho}_w^2$ as

$$\widehat{\rho}_w^2 \equiv \sum_{\ell=1}^{N_{\text{seg}}} w_{\ell} \rho_{\ell}^2, \quad (21)$$

which reduces to the unweighted semi-coherent signal power $\widehat{\rho}^2$ when dropping the weights w_{ℓ} .

B. Parameter-space metrics

Due to the high computational cost of wide parameter-space CW searches, a grid of templates with finite spacing is used to cover the selected parameter-space region. For this reason, the values of the searched parameters will not be equal to the parameters of a possible astrophysical signal. The (coherent) mismatch μ describes the relative loss of signal power $\rho_0^2 \equiv \rho^2(\mathcal{A}_s, \lambda_s; \lambda_s)$ due to computing the coherent detection statistic at offset phase-evolution parameters $\lambda = \lambda_s + \Delta\lambda$ with offset signal power $\rho_{\Delta\lambda}^2 \equiv \rho^2(\mathcal{A}_s, \lambda_s; \lambda)$, i.e.

$$\mu \equiv 1 - \frac{\rho_{\Delta\lambda}^2}{\rho_0^2}, \quad (22)$$

which ranges from 0 (fully recovered signal power) to 1 (no recovered signal power).

The mismatch μ can be approximated by a Taylor expansion of the signal power around the signal parameters (where the mismatch attains a minimum of 0), keeping terms only up to second order [6]:

$$\mu \approx g_{ij} \Delta\lambda^i \Delta\lambda^j + \mathcal{O}(\Delta\lambda^3), \quad (23)$$

where g_{ij} is the parameter-space *metric* and i and j are indices over the phase-evolution parameters. This metric mismatch is just the first term in the expansion, which is a quadratic function of the offset $\Delta\lambda$ and can therefore be larger than 1.

It has been shown that the metric mismatch is typically a good approximation of the true mismatch μ of Eq. (22) up to mismatches of $\mu \gtrsim 0.1$ [6, 25], above which it starts to overestimate the true mismatch. The metric is useful to build template banks of given maximal mismatch and one can estimate the resulting number of templates \mathcal{N} needed to cover a parameter-space region \mathcal{R} by an expression of the form (neglecting boundary effects) [26]:

$$\mathcal{N} \propto \int_{\mathcal{R}} \sqrt{\det(g_{ij})} d\lambda. \quad (24)$$

The most general form of the metric, as defined by Taylor-expanding Eq. (22), results in the \mathcal{F} -statistic metric $g_{ij}^{\mathcal{F}}(\cos \iota, \psi; \lambda)$, which depends on the subset $\{\cos \iota, \psi\}$ of the four signal amplitude parameters \mathcal{A}_s . An explicit expression for this \mathcal{F} -statistic metric can be obtained [6] as:

$$g_{ij}^{\mathcal{F}}(\cos \iota, \psi; \lambda) = \frac{\alpha_1 m_{1;ij} + \alpha_2 m_{2;ij} + 2\alpha_3 m_{3;ij}}{g^2}, \quad (25)$$

in terms of the amplitude angle functions $\alpha_i(\cos \iota, \psi)$ defined in Eq. (15), and the matrices

$$\begin{aligned} m_{1;ij} &\equiv \langle a^2 \partial_i \phi \partial_j \phi \rangle - \frac{A \langle ab \partial_i \phi \rangle \langle ab \partial_j \phi \rangle + B \langle a^2 \partial_i \phi \rangle \langle a^2 \partial_j \phi \rangle - 2C \langle a^2 \partial_i \phi \rangle \langle ab \partial_j \phi \rangle}{D}, \\ m_{2;ij} &\equiv \langle b^2 \partial_i \phi \partial_j \phi \rangle - \frac{A \langle b^2 \partial_i \phi \rangle \langle b^2 \partial_j \phi \rangle + B \langle ab \partial_i \phi \rangle \langle ab \partial_j \phi \rangle - 2C \langle ab \partial_i \phi \rangle \langle b^2 \partial_j \phi \rangle}{D}, \\ m_{3;ij} &\equiv \langle ab \partial_i \phi \partial_j \phi \rangle - \frac{A \langle ab \partial_i \phi \rangle \langle b^2 \partial_j \phi \rangle + B \langle ab \partial_i \phi \rangle \langle a^2 \partial_j \phi \rangle - C [\langle b^2 \partial_i \phi \rangle \langle a^2 \partial_j \phi \rangle + \langle ab \partial_i \phi \rangle \langle ab \partial_j \phi \rangle]}{D}, \end{aligned} \quad (26)$$

where $\partial_i \phi \equiv \frac{\partial \phi}{\partial \lambda^i}$ are the partial phase derivatives for the phase-evolution parameters λ^i .

The signal amplitude parameters $\cos \iota$ and ψ are generally unknown, therefore the practical usefulness of this metric is somewhat limited. One level of simplification consists in an amplitude-“average” form of the \mathcal{F} -

statistic metric, $g_{ij}^{\bar{\mathcal{F}}}$, which was obtained [6] in the form

$$g_{ij}^{\bar{\mathcal{F}}}(\lambda) = \frac{B m_{1;ij} + A m_{2;ij} - 2C m_{3;ij}}{2D}. \quad (27)$$

However, the most commonly-used approximation is the *phase metric* g_{ij}^{ϕ} (initially proposed in [27]), which is obtained by neglecting the signal amplitude modulation,

resulting in the simpler expression

$$g_{ij}^{\phi}(\lambda) = \langle \partial_i \phi \partial_j \phi \rangle - \langle \partial_i \phi \rangle \langle \partial_j \phi \rangle. \quad (28)$$

The semi-coherent metric is typically obtained by averaging the coherent metrics over segments, namely

$$\widehat{g}_{ij} = \frac{1}{N_{\text{seg}}} \sum_{\ell} g_{ij,\ell}, \quad (29)$$

which can be derived under the assumption of *constant per-segment signal power* (see for example [8] or [7]).

III. GENERALIZED PARAMETER-SPACE METRICS

In this section we derive more general expressions for the various parameter-space metrics and discuss improvements in their implementation, in order to take into account data gaps and non-stationarities. This results in more accurate and robust parameter-space metrics, which will be tested numerically in Sec. IV.

A. Data gaps and varying noise floor

The metric expressions in Eqs. (25), (27), and (28) are typically computed numerically. However, current metric implementations in the \mathcal{F} -statistic context, including the main implementation in *UniversalDopplerMetric* of *lalsuite* [28], tend to implement the average Eq. (9) as a simple (unweighted) time-average over the full observation span T of a segment, i.e., $\langle Q \rangle \approx 1/T \int_0^T Q(t) dt$, without taking into account data gaps or varying noise floors². There is some support for differing noise-levels between detectors (see Eq. (59) in [6]), but this does not include noise-floor variations over time and is only implemented in the \mathcal{F} -statistic metrics $g^{\mathcal{F}}$ and $g^{\overline{\mathcal{F}}}$, not the phase metric g^{ϕ} .

In order to take into account data gaps and varying noise floors in the metric, we only need to use the full expression Eq. (9) for the weighted per-SFT average, which already incorporates these effects. We can see that SFTs with a higher noise floor $\mathcal{S}_{X\alpha}$ will contribute less to the metric integral. Therefore adding noisier data (e.g., from a less sensitive previous observing run) will not improve the parameter-space resolution as much as the idealized metrics would predict (e.g., a linear scaling with the observation time for frequency resolution, for example, see Eq. (43) of [30]). The effects of this more general implementation will be illustrated in Sec. IV.

B. New marginalized \mathcal{F} -statistic metric

As discussed in Sec. IIB, the “average” \mathcal{F} -statistic metric $g^{\mathcal{F}}$ in [6] is obtained as the midpoint between mismatch extrema of $g^{\mathcal{F}}$ over $\cos \iota, \psi$. A more natural approach consists of marginalizing the \mathcal{F} -statistic metric $g^{\mathcal{F}}(\cos \iota, \psi; \lambda)$ over the unknown amplitude parameters $\{\cos \iota, \psi\}$ using their physical ignorance priors $P(\cos \iota, \psi) = 1/\pi$, corresponding to isotropic axis orientation of the CW source (e.g., see [20]).

We define the *marginalized \mathcal{F} -statistic metric* $g^{(\mathcal{F})}$ as

$$g_{ij}^{(\mathcal{F})}(\lambda) \equiv \langle g_{ij}^{\mathcal{F}} \rangle_{\cos \iota, \psi} = \frac{1}{\pi} \int_{-1}^1 d \cos \iota \int_{-\pi/4}^{\pi/4} d\psi g^{\mathcal{F}}(\cos \iota, \psi; \lambda), \quad (30)$$

which can be approximated (see Sec. B) as

$$g_{ij}^{(\mathcal{F})} \approx \frac{m_{1;ij} + m_{2;ij}}{A + B}. \quad (31)$$

This expression can be substantially more accurate than the “average” \mathcal{F} -statistic metric $g^{\mathcal{F}}$, especially for short coherent segments, as shown in Sec. IV (e.g., see top panels in Figs. 3 and 4).

The marginalized metric $g^{(\mathcal{F})}$ does not involve the inverse (sub)-determinant D^{-1} , contrary to the “average” $g^{\mathcal{F}}$ of Eq. (27), which can lead to numerical problems for short segments when $D \rightarrow 0$ (see [31]).

C. Generalized semi-coherent metric

The usual expression Eq. (29) for the semi-coherent metric, which was originally derived in [5] and is commonly found in the literature (e.g., see [7, 8]), is derived under the assumption of constant signal power ρ_{ℓ}^2 over all segments. However, this is not generally a good approximation due to varying (i) antenna-patterns A, B, C , (ii) data amounts T_{data} and (iii) noise-floors \mathcal{S} over segments, as seen from Eq. (13) and Fig. 1.

A more accurate semi-coherent metric can be derived by relaxing this assumption. The following derivation is written in terms of the general *weighted* semi-coherent $\widehat{\mathcal{F}}_{\text{w}}$ -statistic of Eq. (17), as the unweighted special case can be recovered by simply dropping the per-segment weights w_{ℓ} .

Starting from the general mismatch definition given by Eq. (22), the semi-coherent mismatch $\widehat{\mu}_{\text{w}}$ can be defined as³

$$\widehat{\mu}_{\text{w}} \equiv 1 - \frac{\widehat{\rho}_{\text{w}\Delta\lambda}^2}{\widehat{\rho}_{\text{w}0}^2}, \quad (32)$$

² However, per-SFT summing and noise-weighting for data gaps and non-constant noise floor *has* been used previously for the cross-correlation statistic, see Sec. IV of [29].

³ Note that *interpolating* semi-coherent statistics require adjustments to the total mismatch, see [8, 14], but those can be equally used with the expressions derived here.

in terms of the offset and perfect-match semi-coherent signal power of Eq. (21) using either offset $\rho_{\Delta\lambda;\ell}^2$ or perfect-match per-segment signal power $\rho_{0;\ell}^2$, respectively. Using the per-segment mismatch μ_ℓ of Eq. (22), we can express the offset per-segment signal power as

$$\rho_{\Delta\lambda;\ell}^2 = (1 - \mu_\ell) \rho_{0;\ell}^2, \quad (33)$$

therefore

$$\hat{\rho}_{w\Delta\lambda}^2 = \sum_{\ell} w_{\ell} \rho_{\Delta\lambda;\ell}^2 = \hat{\rho}_{w0}^2 - \sum_{\ell} w_{\ell} \rho_{0;\ell}^2 \mu_{\ell}, \quad (34)$$

and substituting into Eq. (32) we obtain

$$\hat{\mu}_w = \frac{1}{N_{\text{seg}}} \sum_{\ell=1}^{N_{\text{seg}}} W_{\ell} \mu_{\ell}, \quad (35)$$

where we defined metric segment weights W_{ℓ} as

$$W_{\ell} \equiv \frac{N_{\text{seg}} w_{\ell} \rho_{0;\ell}^2}{\hat{\rho}_{w0}^2}, \quad (36)$$

with the usual weight normalization of $\sum_{\ell} W_{\ell} = N_{\text{seg}}$. As mentioned before, the ‘‘classic’’ semi-coherent metric expression given by Eq. (29) can be recovered under the assumption of constant (weighted) signal power over segments, i.e., $W_{\ell} = 1$.

Applying the metric expansion of Eq. (23) for the \mathcal{F} -statistic metric $g_{ij,\ell}^{\mathcal{F}}$, we find

$$\hat{\mu}_w \approx \hat{g}_{w;ij}^{\mathcal{F}} \Delta\lambda^i \Delta\lambda^j + \mathcal{O}(\Delta\lambda^3), \quad \text{with} \quad (37)$$

$$\hat{g}_{w;ij}^{\mathcal{F}} \equiv \frac{1}{N_{\text{seg}}} \sum_{\ell} W_{\ell} g_{ij,\ell}^{\mathcal{F}}. \quad (38)$$

As noted before in Sec. II B, however, this expression is not typically usable in practice, because both the metric weights W_{ℓ} and the \mathcal{F} -statistic metric $g^{\mathcal{F}}$ depend on the unknown signal amplitude parameters $\{\cos \iota, \psi\}$. The most natural approach again is to marginalize over them using physical priors, as discussed as in Sec. III B, and using the same marginalization approximation as before (see Sec. C for details), we obtain the general result

$$\hat{g}_{w;ij}(\lambda) \approx \frac{1}{N_{\text{seg}}} \sum_{\ell=1}^{N_{\text{seg}}} \varpi_{\ell} g_{ij,\ell}(\lambda), \quad (39)$$

in terms of the marginalized *metric segment weights*

$$\varpi_{\ell} \propto w_{\ell} \gamma_{\ell} (A_{\ell} + B_{\ell}), \quad (40)$$

with standard weight normalization $\sum_{\ell} \varpi_{\ell} = N_{\text{seg}}$.

There are two important cases to distinguish, namely whether the underlying semi-coherent statistic is weighted by w_{ℓ} or not (i.e., dropping w_{ℓ} in the above expressions). The explicit metric weights for two cases are therefore

$$\varpi_{\ell} = \begin{cases} k' w_{\ell}^2 & \text{for weighted } \hat{\mathcal{F}}_w, \\ w_{\ell} & \text{for unweighted } \hat{\mathcal{F}}, \end{cases} \quad (41)$$

in terms of the segment weights w_{ℓ} given in Eq. (19).

For the unweighted $\hat{\mathcal{F}}$ -statistic the metric weights are therefore equal to the statistic weights w_{ℓ} derived in [18], while the metric weights for the weighted $\hat{\mathcal{F}}_w$ -statistic are proportional to the *squared* statistic weights.

A potential practical difficulty introduced by these metric weights is an additional sky-position dependency (via the antenna-pattern coefficients A, B), even if the per-segment metric itself was constant over the sky. This can complicate template-bank placement, but one would likely still reap benefits from using sky-marginalized weights instead, namely $\langle \varpi_{\ell} \rangle_{\text{sky}} \propto \{\gamma_{\ell}^2, \gamma_{\ell}\}$ (for weighted and unweighted statistics, respectively), therefore still accounting for the variations in data-quality and quantity over segments illustrated in Fig. 1.

IV. NUMERICAL TESTS

In this section we will test the accuracy of the generalized parameter-space metrics by comparing them to mismatch estimations made with the metrics that do not take into account data gaps, non-constant noise floors, and signal power variability between segments. We compute the relative error ε between (i) the predicted mismatch values and (ii) actual mismatch values obtained from \mathcal{F} -statistic calculations with simulated signals, as for example done in [6, 8]:

$$\varepsilon = 2 \frac{\mu - m}{\mu + m}, \quad (42)$$

where μ is given by Eq. (22) and m by Eq. (23) (we did not use the spherical ansatz of [32] in order keep the interpretation of our results simpler).

We will also compare the ratio r of (square root) determinants between the new and previous metrics:

$$r = \sqrt{\frac{\det(g_{n;ij})}{\det(g_{p;ij})}}, \quad (43)$$

where $g_{n;ij}$ represents the new generalized metrics and $g_{p;ij}$ the previous idealized metrics. This comparison is interesting because a higher determinant indicates that a greater number of templates are required to cover a given parameter-space region, as shown by Eq. (24). In this way we can check whether building template banks with more realistic metrics requires more or less templates.

In these tests we generate 100 simulated CW signals (thus generating a total of 100 r values for each test) with isotropically distributed amplitude parameters and sky positions, fixed values for the time of ascending node and for the reference time (both equal to the mid-time of the dataset, i.e. $t_{\text{asc}} = t_r = t_m$), and with uniform distributions in these intervals: $f_0 = [99.9, 100.1]$ Hz, $f_1 = [-10^{-10}, 10^{-10}]$ Hz/s, $f_2 = [-10^{-17}, 10^{-17}]$ Hz/s², $a_p = [10, 40]$ l-s, $P_{\text{orb}} = [15, 45]$ days, $e = [0, 0.1]$, $\omega = [0, 2\pi)$. The parameter-space metrics are calculated at the true parameters of each signal.

For each of these signals we obtain 100 points with displaced parameters where the mismatches μ and m are calculated (thus generating a total of 10000 ε values for each test). In order to generate the displaced points we create an ellipsoid described by the \mathcal{F} -statistic metric $g_{ij}^{\mathcal{F}}$ of Eq. (25), where i and j go only over the $\{f_0, f_1, f_2\}$ parameters (we use these parameters for simplicity, since other parameters generate non-constant metrics that make the comparison of the relative error less straightforward). This ellipsoid has a squared radius of $m_{\mathcal{R}} = 0.2$, and is centered on the parameters of the simulated signal. We draw random points from this ellipsoid with a uniform distribution (as explained in Sec. IV C of [33]).

We also generate mismatch heatmaps to graphically illustrate the improvement of the new parameter-space metrics. To obtain these heatmaps we instead generate a grid of 31×31 points in the $\{f_0, f_1\}$ parameters for a single simulated signal, with a maximum mismatch that defines the grid resolution of $m_0 = 0.001$ (using the \mathcal{F} -statistic metric $g_{ij}^{\mathcal{F}}$ of Eq. (25)).

We will firstly generate datasets with a single segment in order to test the coherent metrics, and then we will generate datasets with multiple segments to test the semi-coherent metrics (both for unweighted and weighted detection statistics). We use segment times of 0.1 days and 10 days.

We have used public data from the O2 and O3 observing runs [9, 10, 34] of the Advanced LIGO detectors, in order to obtain setups with realistic datasets (i.e. distribution of SFT timestamps and ASD values). Each of the simulated CW signals is generated with duty cycles and ASD values equal to those of the O2/O3 datasets. Since the datasets that we generate are noiseless, the ASD values are used as known quantities to calculate the detection statistics.

To carry out these tests we have modified the *lalsuite* code related to the parameter-space metrics, and have used the *SWIGLAL* wrapper [35] to interface it with custom Python code. When interpreting Figs. 2, 3, and 4, one should remember that the metric mismatch is a second-order Taylor approximation that overestimates (so the relative error ε becomes negative) the real mismatch for $\mu \gtrsim 0.1$.

A. Coherent metric

The results from the tests with a single segment are shown in Fig. 2.

Regarding the relative error ε , we observe a clear improvement in the three different datasets when using the generalized metrics, since the boxes have a smaller spread and are closer to zero. It can be seen that the O2+O3 dataset (which has a big gap between the observing runs and a large difference in noise floors) shows the biggest disagreement between idealized and generalized metrics. It can also be seen that the difference between the met-

rics (phase, \mathcal{F} -statistic, etc.) is almost negligible, due to the long duration of the datasets.

Regarding the determinant ratio r , the tests do not show a clear effect: the O2 dataset shows a ratio bigger than one, while the O2+O3 dataset shows a ratio smaller than one. We observe agreement between the ratio of the different metric pairs.

The heatmap shows the almost perfect agreement between the generalized \mathcal{F} -statistic metric and its respective mismatch ellipse, while the idealized metric fails to predict this ellipse with the same accuracy.

B. Semi-coherent metric

The results from the tests with multiple segments and a non-weighted \mathcal{F} -statistic are shown in Fig. 3.

Regarding the relative error ε , it can be seen that the cases with $T_{\text{seg}} = 0.1$ days have a bigger difference between the phase and \mathcal{F} -statistic metrics than the cases with $T_{\text{seg}} = 10$ days. Furthermore, for the shorter segments a clear improvement between the generalized “average” \mathcal{F} -statistic metric and the generalized marginalized \mathcal{F} -statistic metric can be seen for the three datasets. For the longer segments, we have a similar situation to the results obtained in the fully coherent case. Again, we observe everywhere an improvement when using the generalized metrics as compared to when using the idealized metrics. The three datasets show comparable results for the shorter segments, while the results have a higher variation when using longer segments.

Regarding the determinant ratio r , we observe a large difference between the results of the three different pair combinations for the short segment time. But given that (as shown in the plots regarding the relative error) the result for the \mathcal{F} -statistic metric is the most accurate, it would seem that the most trustable observation is that for the three datasets there is clear reduction in the required number of templates. For the longer segment time, the results between the different metric pairs are similar, and also show that a reduction in the number of templates is expected when using the generalized metrics.

The heatmaps show again almost perfect agreement between the generalized \mathcal{F} -statistic metric and the respective mismatch ellipse, accurately predicting its orientation and size. The disagreement for the idealized metric in this example is greater than for the previous coherent example. Also, the disagreement is bigger for the shorter segment case, agreeing with the results shown in the left column plots.

C. Semi-coherent metric with weighted detection statistic

The results from the tests with multiple segments and a weighted \mathcal{F} -statistic are shown in Fig. 4.

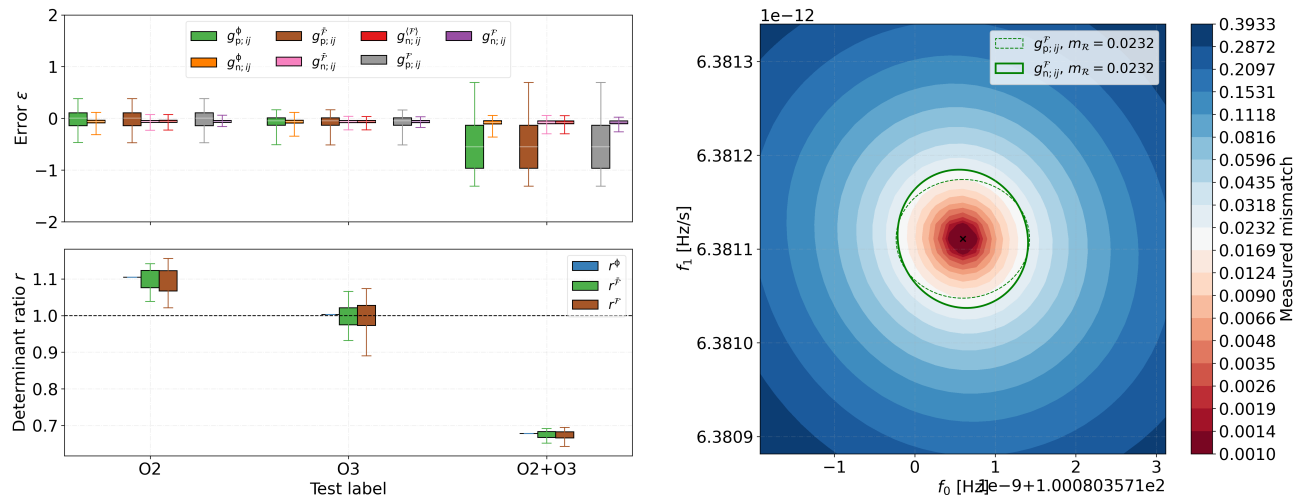


FIG. 2: The left column shows the relative error and the determinant ratio for the different coherent tests, while the right column shows a mismatch heatmap for one simulated signal with the previous (dashed green ellipse) and new (green ellipse) \mathcal{F} -statistic metrics at a given mismatch value (for O2+O3). The boxes in the left column enclose the (25, 75) percentile with the error bars reaching the minimum and maximum values of the distribution and a thin white line showing the median, and each colored box (with 10000 results for ε and 100 for r) represents a different metric (sorted following the legend from top-down and then left-right).

Regarding the relative error ε , we observe similar results to the previous non-weighted semi-coherent section, but where the differences between the idealized and generalized metrics have slightly increased due to the effect of the squared metric weights.

Regarding the determinant ratio r , the plots show more extreme values, reaching 0.5 for the case with a shorter segment time, implying a reduced number of templates.

The heatmaps show again good agreement between the new \mathcal{F} -statistic metric and their respective mismatch ellipses. In this case, due to the squared metric weights that are not applied in the previous idealized metrics, the differences between the metrics are the largest, specially in the case with the shorter segments. A comparison between these heatmaps and those of Fig. 3 clearly shows that the ellipses get more elongated, with the difference coming from using weights in the detection statistic.

As a practical example showcasing the advantage of using a more realistic parameter-space metric, Fig. 5 shows three mismatch distributions obtained after building three A^* lattice grids over the $\{f_0, f_1, f_2\}$ parameters and finding the minimum mismatch achieved in the grid using the O3 dataset. We repeat this for 100 different signals, randomly shifting the center of the lattice for each simulated signal. The $\hat{g}_{n,w;ij}^\phi$ lattice grid is built by requiring a maximum mismatch $m_0 = 0.375$, while $m_0 = 0.3$ for the $\hat{g}_{p;ij}^\phi$ lattice grid. These two m_0 values have been chosen so that the average mismatch is almost equal between the generalized and idealized metrics, as the figure shows. The ratio of number of templates between these two grids is 0.77 ± 0.04 (the grids have enough

points so that border effects can be neglected), showing a non-negligible decrease of the required number of templates while keeping almost the same mismatch level. We have also obtained results for $\hat{g}_{n,w;ij}^\phi$ using a $m_0 = 0.3$ $\hat{g}_{n,w;ij}^\phi$ grid, which shows that when the same maximum mismatch is used to construct both lattice grids, the mismatch distribution of $\hat{g}_{n,w;ij}^\phi$ gets slightly displaced to lower mismatch values, but the ratio of number of templates is then increased.

V. CONCLUSIONS

In this paper we have generalized the expressions for the parameter-space metrics related to the \mathcal{F} -statistic. We have shown that for realistic datasets with data gaps and a varying noise floor the idealized expressions can fail to predict the shape and size of the \mathcal{F} -statistic mismatch, and that our new expressions are more accurate. We have presented a new expression describing a marginalized (over the unknown neutron star orientation vector) \mathcal{F} -statistic metric, which also improves over the previous “average” \mathcal{F} -statistic metric. Finally, we have derived an expression for the semi-coherent metric that properly takes into account the variability of the signal power across different segments by applying weights, and we have derived the correct expression for detection statistics that are weighted. We have shown that these generalized semi-coherent metrics better predict the mismatch of the semi-coherent \mathcal{F} -statistic when using realistic datasets.

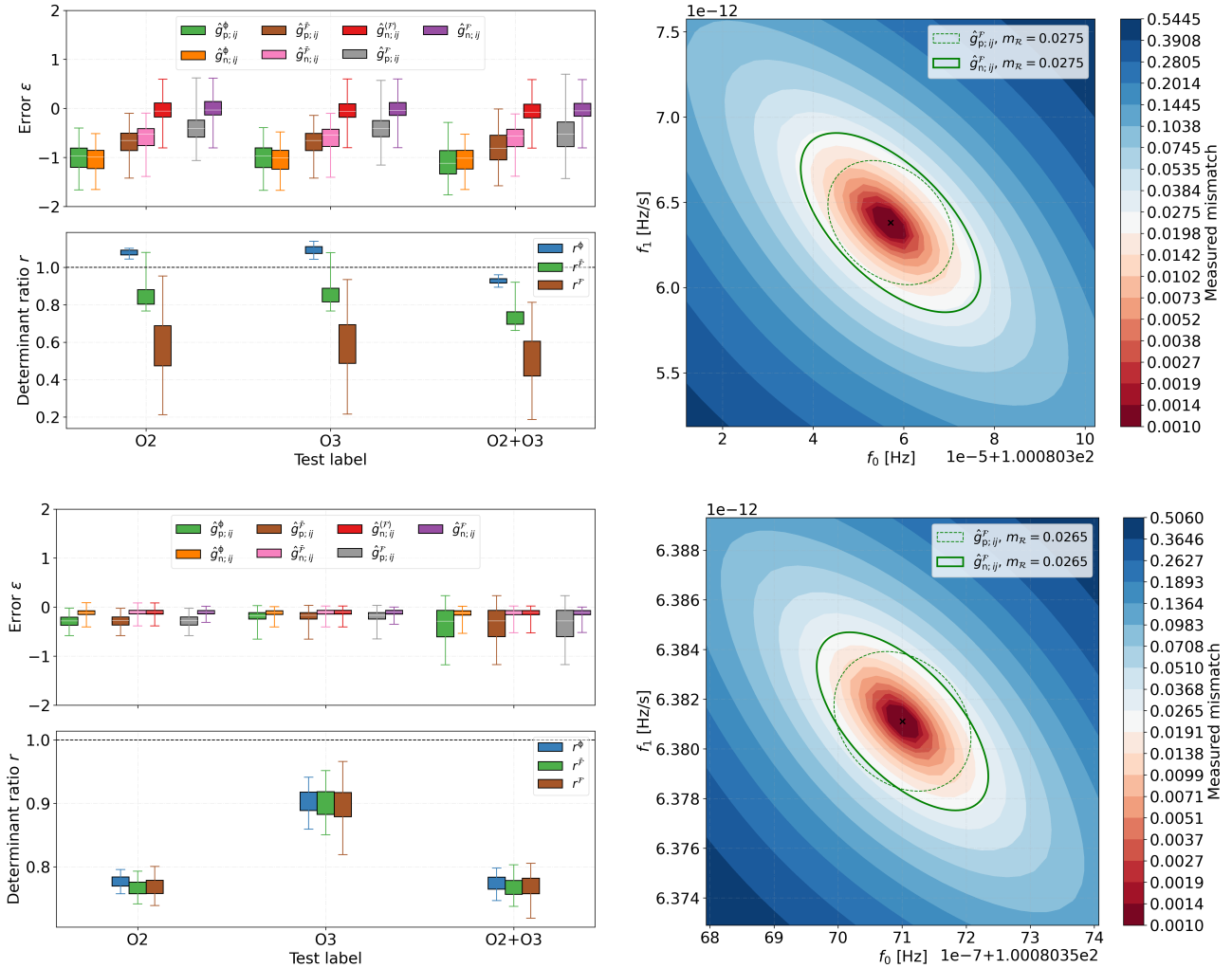


FIG. 3: The left column shows the relative error and the determinant ratio for the different semi-coherent (without detection statistic weights) tests, while the right column shows two mismatch heatmaps for one simulated signal with the previous (dashed green ellipse) and new (green ellipse) \mathcal{F} -statistic metrics at a given mismatch value (for O2+O3). The first row shows the results for $T_{\text{seg}} = 0.1$ days, while the second row shows $T_{\text{seg}} = 10$ days. The boxes in the left column enclose the (25, 75) percentile with the error bars reaching the minimum and maximum values of the distribution and a thin white line showing the median, and each colored box (with 10000 results for ϵ and 100 for r) represents a different metric (sorted following the legend from top-down and then left-right).

Although we have not found analytical expressions for the generalized parameter-space metrics, they can be numerically obtained. A disadvantage of the new expressions is that since they need to be integrated SFT by SFT they require a higher computational effort than their idealized counterparts, which might complicate their application in case many metrics need to be calculated, such as in an injection campaign with thousands of signals.

We have also shown that for semi-coherent searches and realistic datasets like the O2 and O3 observing runs, using the new parameter-space metrics could bring down the required number of templates (keeping the same maximum mismatch) by factors between 0.6 and 0.9 (we have

only investigated this for a grid over the $\{f_0, f_1, f_2\}$ parameters). This could be converted to a sensitivity improvement if the saved computational cost is spent in using a finer template bank, for example.

In this paper we have not explored the behavior of the metric for segment times shorter than 0.1 days. For this segment time we have observed a larger difference between the idealized and the generalized metrics, due to the greater variability of the signal power in each segment. We have also observed that the variance of the results is larger. It has been recently shown that there are more sensitive detection statistics than the \mathcal{F} -statistic for short segment times [23, 31], but we leave this regime

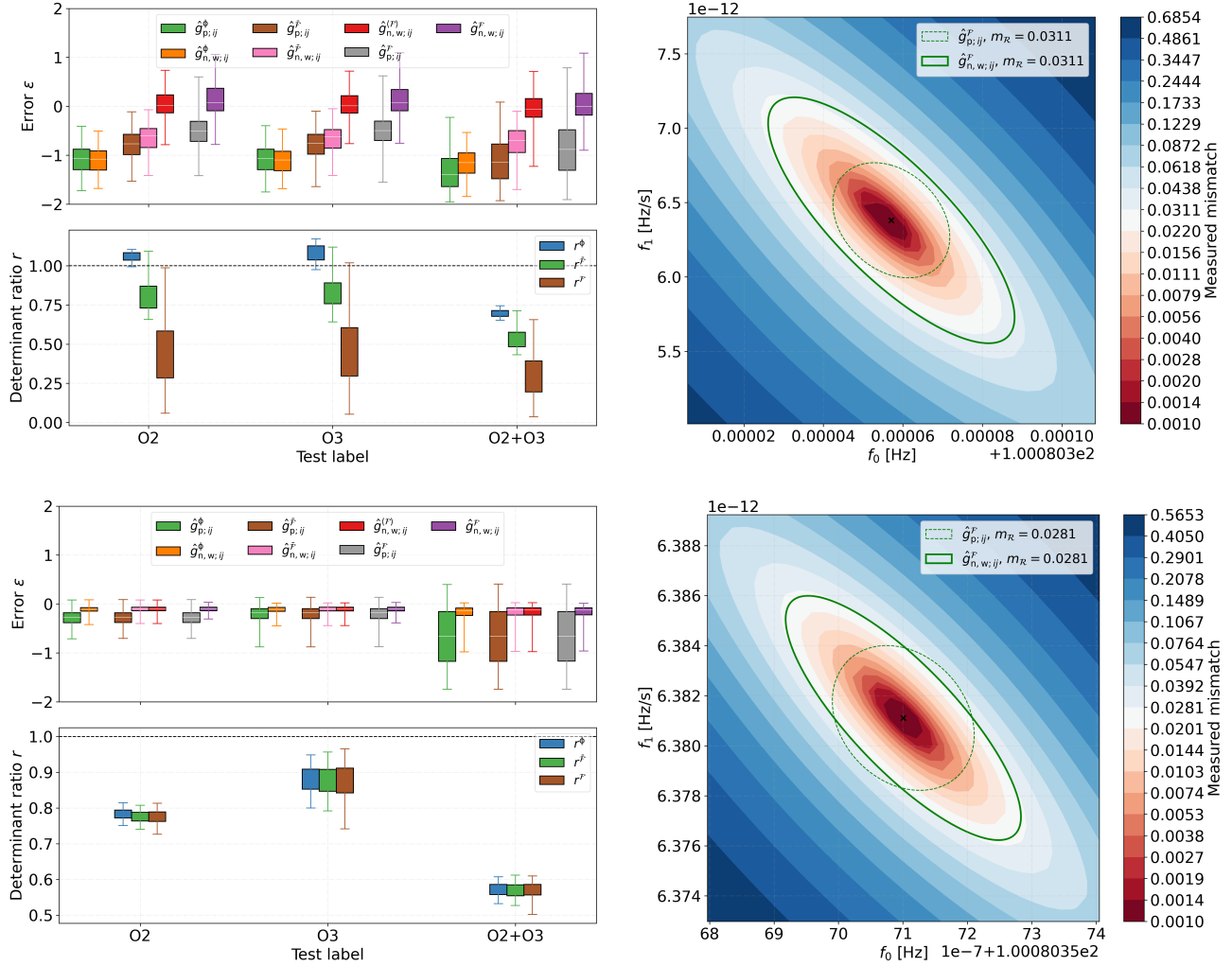


FIG. 4: The left column shows the relative error and the determinant ratio for the different semi-coherent (with detection statistic weights) tests, while the right column shows two mismatch heatmaps for one simulated signal with the previous (dashed green ellipse) and new (green ellipse) \mathcal{F} -statistic metrics at a given mismatch value (for O2+O3). The first row shows the results for $T_{\text{seg}} = 0.1$ days, while the second row shows $T_{\text{seg}} = 10$ days. The boxes in the left column enclose the (25, 75) percentile with the error bars reaching the minimum and maximum values of the distribution and a thin white line showing the median, and each colored box (with 10000 results for ϵ and 100 for r) represents a different metric (sorted following the legend from top-down and then left-right).

for future investigations. It would also be interesting to investigate the parameter-space metric of the detection statistic that includes a non-Gaussian line hypothesis such as [36]. We have only tested the new generalized metrics for the $\{f_0, f_1, f_2\}$ parameters, but we believe that the improvements shown in our tests would also apply for other parameters like the sky position or the ones describing the binary orbit. We also leave this for future research.

ACKNOWLEDGMENTS

This project has received funding from the European Union’s Horizon 2020 research and innovation programme under the Marie Skłodowska-Curie grant agreement number 101029058.

This work has utilized the ATLAS computing cluster at the MPI for Gravitational Physics Hannover.

This research has made use of data or software obtained from the Gravitational Wave Open Science Center (gwosc.org), a service of the LIGO Scientific Collaboration, the Virgo Collaboration, and KAGRA [37].

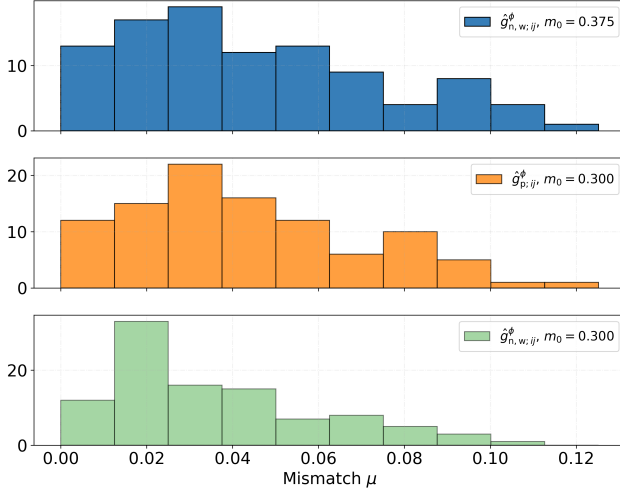


FIG. 5: Histograms showing the mismatch distribution for 100 different signals searched with an A^* lattice grid built with three different lattices: blue (top) shows $\hat{g}_{n,w;ij}^\phi$ with $m_0 = 0.375$, orange (center) shows $\hat{g}_{p;ij}^\phi$ with $m_0 = 0.3$, and green (bottom) shows $\hat{g}_{n,w;ij}^\phi$ with $m_0 = 0.3$.

Appendix A: Weighted semi-coherent signal power

Let us look in more detail at the (perfect-match) weighted semi-coherent signal power $\hat{\rho}_{w0}^2$ of Eq. (21), by inserting the per-segment matched signal power $\rho_{0;\ell}^2$ of Eq. (13), which leads to

$$\begin{aligned} \hat{\rho}_{w0}^2 &= \sum_{\ell} w_{\ell} \rho_{0;\ell}^2 \\ &= h_0^2 \sum_{\ell} w_{\ell} \gamma_{\ell} (\alpha_1 A_{\ell} + \alpha_2 B_{\ell} + 2\alpha_3 C_{\ell}). \end{aligned} \quad (\text{A1})$$

Using Eq. (7) we can see that semi-coherent data factor $\hat{\gamma}$ is self-consistently defined as

$$\hat{\gamma} \equiv \mathcal{S}^{-1} T_{\text{data}} = \sum_{\ell} \gamma_{\ell}, \quad (\text{A2})$$

where \mathcal{S} , defined in Eq. (8), and T_{data} now refer to the full dataset over all segments. We can therefore write the weighted signal power Eq. (A1) in the form

$$\hat{\rho}_{w0}^2 = h_0^2 \hat{\gamma} \hat{g}_w^2, \quad (\text{A3})$$

where we defined the (weighted) semi-coherent geometric response function as

$$\hat{g}_w^2 \equiv \alpha_1 \hat{A}_w + \alpha_2 \hat{B}_w + 2\alpha_3 \hat{C}_w, \quad (\text{A4})$$

in terms of the (weighted) semi-coherent antenna-pattern coefficients

$$\begin{aligned} \hat{\gamma} \hat{A}_w &\equiv \sum_{\ell} w_{\ell} \gamma_{\ell} A_{\ell}, \\ \hat{\gamma} \hat{B}_w &\equiv \sum_{\ell} w_{\ell} \gamma_{\ell} B_{\ell}, \\ \hat{\gamma} \hat{C}_w &\equiv \sum_{\ell} w_{\ell} \gamma_{\ell} C_{\ell}. \end{aligned} \quad (\text{A5})$$

As expected, the above weighted expressions reduce to the standard semi-coherent forms when dropping the weights w_{ℓ} .

Appendix B: Amplitude-marginalizing the coherent \mathcal{F} -statistic metric

In order to marginalize the \mathcal{F} -statistic metric $g_{ij}^{\mathcal{F}}$ of Eq. (25) over $\cos \iota, \psi$, we start by writing it more compactly as

$$g_{ij}^{\mathcal{F}}(\cos \iota, \psi; \lambda) = \sum_{k=1}^3 m_{k;ij}(\lambda) \frac{\alpha_k(\cos \iota, \psi)}{g^2(\cos \iota, \psi; \lambda)}, \quad (\text{B1})$$

where for convenience of notation we defined $\alpha_1 \equiv \alpha_1$, $\alpha_2 \equiv \alpha_2$ and $\alpha_3 \equiv 2\alpha_3$. With the marginalization integrals over $\cos \iota, \psi$ of Eq. (30), we can write

$$g_{ij}^{(\mathcal{F})}(\lambda) \equiv \langle g_{ij}^{\mathcal{F}} \rangle_{\cos \iota, \psi} = \sum_{k=1}^3 m_{k;ij}(\lambda) K_k(\lambda), \quad (\text{B2})$$

in terms of the three marginalization integrals K_k , for which we propose the approximation

$$K_k(\lambda) \equiv \left\langle \frac{\alpha_k}{g^2} \right\rangle_{\cos \iota, \psi} \approx \frac{\langle \alpha_k \rangle_{\cos \iota, \psi}}{\langle g^2 \rangle_{\cos \iota, \psi}}, \quad (\text{B3})$$

replacing the average of the ratio by the ratio of averages. We will test the accuracy of this approximation numerically in Sec. D. We can use the known averages (e.g., [19]) of $\langle \alpha_1 \rangle_{\cos \iota, \psi} = \langle \alpha_2 \rangle_{\cos \iota, \psi} = 2/5$ and $\langle \alpha_3 \rangle_{\cos \iota, \psi} = 0$, to obtain $\langle g^2 \rangle_{\cos \iota, \psi} = \frac{2}{5}(A+B)$ from Eq. (14), and therefore

$$K_1 \approx K_2 \approx \frac{1}{A+B}, \quad K_3 \approx 0. \quad (\text{B4})$$

Inserting this approximation into Eq. (B2) we now find

$$g_{ij}^{(\mathcal{F})} \approx \frac{m_{1;ij} + m_{2;ij}}{A+B}, \quad (\text{B5})$$

as stated in Eq. (31).

Appendix C: Amplitude marginalization of semi-coherent metrics

Here we consider the amplitude-marginalization of the most general semi-coherent metric $\hat{g}_{w;ij}^{\mathcal{F}}$ of Eq. (38) for

(weighted) \mathcal{F} -statistics. We can write this amplitude-marginalized metric as

$$\begin{aligned}\widehat{g}_{w;ij}^{(\mathcal{F})} &\equiv \langle \widehat{g}_{w;ij}^{\mathcal{F}} \rangle_{\cos \iota, \psi} \\ &= \frac{1}{N_{\text{seg}}} \sum_{\ell} \langle W_{\ell} g_{ij,\ell}^{\mathcal{F}} \rangle_{\cos \iota, \psi} \\ &= \sum_{k=1}^3 \sum_{\ell=1}^{N_{\text{seg}}} w_{\ell} m_{k;ij,\ell} \left\langle \frac{\rho_{0;\ell}^2}{\widehat{\rho}_{w0}^2} \frac{\alpha_k}{g_{\ell}^2} \right\rangle_{\cos \iota, \psi},\end{aligned}\quad (\text{C1})$$

where in the last line we substituted the metric weights W_{ℓ} of Eq. (36) and the per-segment \mathcal{F} -statistic metric $g_{ij,\ell}^{\mathcal{F}}$ of Eq. (B1). Using the explicit signal-power expression Eq. (13) with Eq. (A3), this leads to

$$\widehat{g}_{w;ij}^{(\mathcal{F})} = \sum_{k\ell} w_{\ell} m_{k;ij,\ell} \frac{\gamma_{\ell}}{\widehat{\gamma}} K_{w;k}, \quad (\text{C2})$$

where we defined (similar to the coherent case given by Eq. (B3)) the marginalization integrals $K_{w;k}$, for which we propose the approximation

$$K_{w;k} \equiv \left\langle \frac{\alpha_k}{\widehat{g}_{\text{w}}^2} \right\rangle_{\cos \iota, \psi} \approx \frac{\langle \alpha_k \rangle_{\cos \iota, \psi}}{\langle \widehat{g}_{\text{w}}^2 \rangle_{\cos \iota, \psi}}, \quad (\text{C3})$$

with the result in the same form as in Sec. B:

$$K_{w;1} \approx K_{w;2} \approx \frac{1}{\widehat{A}_{\text{w}} + \widehat{B}_{\text{w}}}, \quad K_{w;3} \approx 0. \quad (\text{C4})$$

Putting this together with Eq. (C2) we obtain the approximation

$$\begin{aligned}\widehat{g}_{w;ij}^{(\mathcal{F})} &\approx \sum_{\ell} w_{\ell} \frac{\gamma_{\ell}}{\widehat{\gamma}} \frac{m_{1;ij,\ell} + m_{2;ij,\ell}}{\widehat{A}_{\text{w}} + \widehat{B}_{\text{w}}} \\ &\approx \sum_{\ell} \left(w_{\ell} \frac{\gamma_{\ell}}{\widehat{\gamma}} \frac{A_{\ell} + B_{\ell}}{\widehat{A}_{\text{w}} + \widehat{B}_{\text{w}}} \right) g_{ij,\ell}^{(\mathcal{F})},\end{aligned}\quad (\text{C5})$$

where in the last line we used the coherent marginalized \mathcal{F} -statistic metric $g_{ij,\ell}^{(\mathcal{F})}$ of Eq. (31). We can see that the weight factor multiplying $g_{ij,\ell}^{(\mathcal{F})}$ corresponds to the (marginalized) metric segment weights ϖ_{ℓ} given in Eq. (40), namely

$$\varpi_{\ell} \equiv k' w_{\ell} \gamma_{\ell} (A_{\ell} + B_{\ell}), \quad (\text{C6})$$

with normalization

$$k' = \frac{N_{\text{seg}}}{\widehat{\gamma} (\widehat{A}_{\text{w}} + \widehat{B}_{\text{w}})}, \quad (\text{C7})$$

satisfying the normalization condition $\sum_{\ell} \varpi_{\ell} = N_{\text{seg}}$. Therefore we can write

$$\widehat{g}_{w;ij}^{(\mathcal{F})} \approx \frac{1}{N_{\text{seg}}} \sum_{\ell} \varpi_{\ell} g_{ij,\ell}^{(\mathcal{F})}, \quad (\text{C8})$$

as stated in Eq. (39).

In order to see that this form of the result also holds true for the phase metric, we first note that

$$\begin{aligned}\langle W_{\ell} \rangle_{\cos \iota, \psi} &= N_{\text{seg}} w_{\ell} \left\langle \frac{\rho_{0,\ell}^2}{\widehat{\rho}_{w0}^2} \right\rangle_{\cos \iota, \psi} \\ &\approx N_{\text{seg}} w_{\ell} \frac{\gamma_{\ell}}{\widehat{\gamma}} \langle g_{\ell}^2 \rangle \\ &= N_{\text{seg}} \frac{w_{\ell} \gamma_{\ell} (A_{\ell} + B_{\ell})}{\widehat{\gamma} (\widehat{A}_{\text{w}} + \widehat{B}_{\text{w}})} \\ &= \varpi_{\ell},\end{aligned}\quad (\text{C9})$$

and therefore the amplitude-marginalized weighted phase-metric is also approximated in the form

$$\begin{aligned}\widehat{g}_{w;ij}^{(\phi)} &\equiv \langle g_{w;ij}^{\phi} \rangle_{\cos \iota, \psi} = \frac{1}{N_{\text{seg}}} \sum_{\ell} \langle W_{\ell} \rangle g_{ij,\ell}^{\phi} \\ &\approx \frac{1}{N_{\text{seg}}} \sum_{\ell} \varpi_{\ell} g_{ij,\ell}^{\phi},\end{aligned}\quad (\text{C10})$$

as stated in Eq. (39).

Appendix D: Testing the amplitude marginalization approximation

We perform numerical tests for the two cases of the coherent approximation given by Eq. (B4) of Sec. B as well as the semi-coherent weighted case of Eq. (C4) of Sec. C. In these tests we compare the true values, computed numerically, to the approximations.

Given K_3 is approximated as 0, we cannot compute a standard relative error, instead we chose a common approximation ‘‘scale’’ of $K_0 \equiv 1/(A + B)$ to compute the relative importance of the absolute deviations in the sum in Eq. (B2), namely

$$\varepsilon_1 \equiv \frac{K_1 - K_0}{K_0}, \quad \varepsilon_2 \equiv \frac{K_2 - K_0}{K_0}, \quad \varepsilon_3 \equiv \frac{K_3}{K_0}. \quad (\text{D1})$$

We have made the same definitions for the semi-coherent weighted case, substituting K_k and ε_k by $K_{w;k}$ and $\varepsilon_{w;k}$.

Fig. 6 shows histograms of these relative deviations computed over randomly chosen sky-positions for different data spans. We see that this approximation tends to only introduce small errors on the order of a few percent for observation times of a day and longer. However, for shorter observations such as $T_{\text{data}} = 1/4$ days, we see that this approximation is less precise, and a different approach might be needed, which is postponed to future work.

REFERENCES

- [1] K. Riles, Living Reviews in Relativity **26**, 3 (2023).
- [2] P. Jaranowski, A. Królak, and B. F. Schutz, Phys. Rev. D **58**, 063001 (1998).

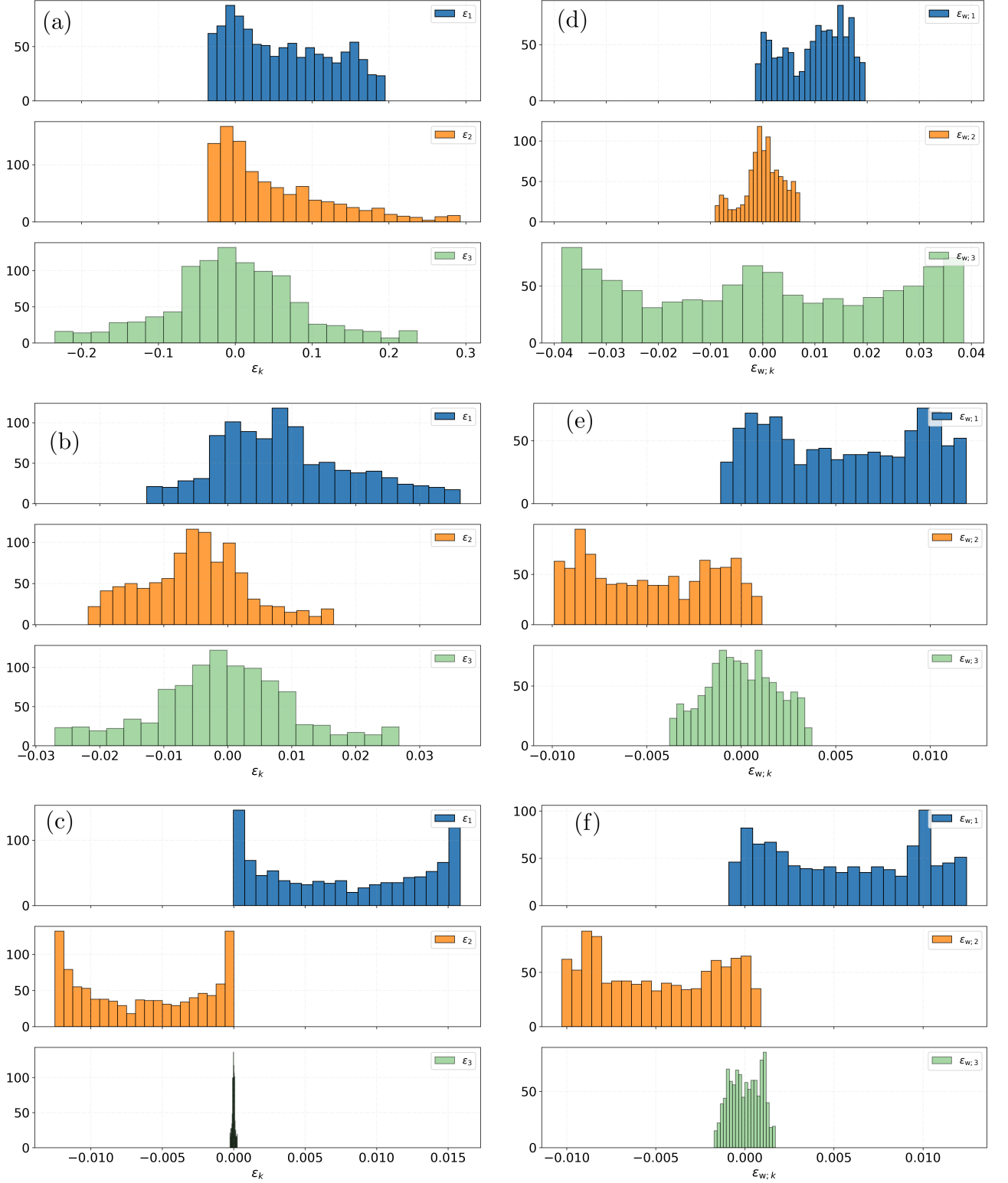


FIG. 6: Histogram showing ε_k , defined in Eq. (D1). The 1000 simulated signals of each histogram are isotropically distributed over the sky. For the left column, the antenna pattern matrix coefficients have been obtained with 1800 s SFTs without gaps from the H1 and L1 detectors with constant and equal noise floors covering (from top row to bottom) 0.25 days (a), 1.2 days (b), and 146 days (c). For the right column, the antenna pattern matrix coefficients have been obtained with 1800 s SFTs from the H1 and L1 detectors belonging to the O3 observing run that have been modified with a time-domain cleaning algorithm [17] with a segment time of (from top row to bottom) $T_{\text{seg}} = 900$ s (d), $T_{\text{seg}} = 1.2$ days (e), and $T_{\text{seg}} = 12.1$ days (f).

- [3] C. Cutler and B. F. Schutz, *Phys. Rev. D* **72**, 063006 (2005).
- [4] K. Wette, *Astroparticle Physics* **153**, 102880 (2023).
- [5] P. R. Brady and T. Creighton, *Phys. Rev. D* **61**, 082001 (2000).
- [6] R. Prix, *Phys. Rev. D* **75**, 023004 (2007).
- [7] H. J. Pletsch, *Phys. Rev. D* **82**, 042002 (2010).
- [8] K. Wette, *Phys. Rev. D* **92**, 082003 (2015).
- [9] LIGO Scientific Collaboration, Virgo Collaboration, and KAGRA Collaboration, **10.7935/nfmt-hm34** (2021).
- [10] LIGO Scientific Collaboration, Virgo Collaboration, and KAGRA Collaboration, **10.7935/pr1e-j706** (2021).
- [11] J. Aasi *et al.*, *Class. Quant. Grav.* **32**, 074001 (2015).
- [12] R. Prix, *Class. Quant. Grav.* **24**, S481 (2007).
- [13] B. Allen, *Phys. Rev. D* **104**, 042005 (2021).
- [14] R. Prix and M. Shaltev, *Phys. Rev. D* **85**, 084010 (2012).
- [15] M. Sieniawska and D. I. Jones, *Monthly Notices of the Royal Astronomical Society* **509**, 5179 (2021).
- [16] J. S. Speagle, *Monthly Notices of the Royal Astronomical Society* **493**, 3132 (2020).
- [17] B. Steltner, M. A. Papa, and H.-B. Eggenstein, *Phys. Rev. D* **105**, 022005 (2022).
- [18] P. B. Covas and R. Prix, *Phys. Rev. D* **106**, 084035 (2022).
- [19] R. Prix, LIGO DCC **T0900149-v6** (2010).
- [20] R. Prix and B. Krishnan, *Class. Quant. Grav.* **26**, 204013 (2009).
- [21] B. Allen and G. Mendell, LIGO DCC **T040164** (2004).
- [22] C. Dreissigacker, R. Prix, and K. Wette, *Phys. Rev. D* **98**, 084058 (2018).
- [23] R. Prix, *Class. Quant. Grav.* **42**, 065006 (2025).
- [24] R. Prix, S. Giampanis, and C. Messenger, *Phys. Rev. D* **84**, 023007 (2011).
- [25] K. Wette and R. Prix, *Phys. Rev. D* **88**, 123005 (2013).
- [26] G. Ashton and R. Prix, *Phys. Rev. D* **97**, 103020 (2018).
- [27] P. R. Brady, T. Creighton, C. Cutler, and B. F. Schutz, *Phys. Rev. D* **57**, 2101 (1998).
- [28] LIGO Scientific Collaboration, Virgo Collaboration, and KAGRA Collaboration, **10.7935/GT1W-FZ16** (2018).
- [29] J. T. Whelan, S. Sundaresan, Y. Zhang, and P. Peiris, *Phys. Rev. D* **91**, 102005 (2015).
- [30] J. Ming, B. Krishnan, M. A. Papa, C. Aulbert, and H. Fehrmann, *Phys. Rev. D* **93**, 064011 (2016).
- [31] P. B. Covas and R. Prix, *Phys. Rev. D* **105**, 124007 (2022).
- [32] B. Allen, *Phys. Rev. D* **100**, 124004 (2019).
- [33] P. B. Covas, R. Prix, and J. Martins, *Phys. Rev. D* **110**, 024053 (2024).
- [34] LIGO Scientific Collaboration, Virgo Collaboration, and KAGRA Collaboration, **10.7935/CA75-FM95** (2019).
- [35] K. Wette, *SoftwareX* **12**, 100634 (2020).
- [36] D. Keitel, R. Prix, M. A. Papa, P. Leaci, and M. Siddiqi, *Phys. Rev. D* **89**, 064023 (2014).
- [37] R. Abbott *et al.*, *The Astrophysical Journal Supplement Series* **267**, 29 (2023).